Thermal behavior of high silica mordenite

(Article begins on next page)

19 September 2024

Thermal behavior of high silica mordenite

RiccardoFantini[a]RossellaArletti[a]SimonaQuartieri[b]MarcoFabbiani[c]SaraMorandi[c]GianmarioMartra[c]FrancescoDi Renzo[d]GiovannaVezzalini[a]

[a]

Abstract

This work studies the thermal stability, heat-induced structural deformations, and dehydration/rehydration dynamics of a synthetic high silica mordenite. It is of special interest because this particular phase has proven to be an ideal host for the encapsulation of several kinds of organic molecules making it a promising scaffold for drug delivery. The dehydration process was followed by thermal analysis, infrared spectroscopy in controlled atmosphere, in situ synchrotron XRPD, and structural refinement. Overall, all the results indicate weak interactions of H_2O molecules with the silicatic mordenite framework and evidence the presence of hydroxyl groups with different condensation responses at high temperature. Infrared characterization highlighted how the desorption of adsorbed H_2O molecules under degassing is already complete at rT. The unit cell parameters exhibit very slow and almost isotropic changes upon heating. Above 550 °C an increase in slope is observed for all parameters. This corresponds to the marked silanol condensation and consequent framework reassessment observed at this temperature by infrared characterization. Overall cell contractions are 0.67%, 1.18%, and 0.81% for a, b, c, respectively and 2.64% for cell volume. HS-MOR undergoes very moderate T induced deformations, indicating a very rigid and stable framework.

Graphical abstract
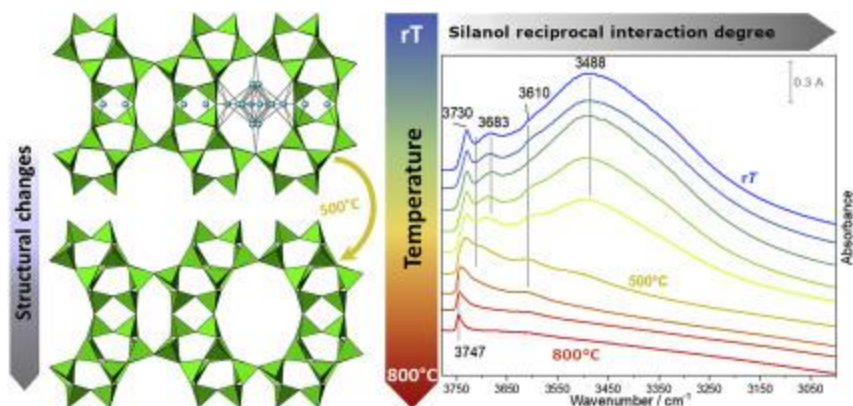
Keywords

1. Introduction

Establishing the thermal stability of a zeolite is of particular importance since its properties can change in the dehydrated/calcined state and under operating conditions. Understanding the mechanisms governing heat-induced structural deformations is crucial for many technological applications, e.g. Ref. [1]. Zeolites are exploited in diverse complex applications, ranging from catalysis to drug delivery. Due to their physicochemical stability, uniform porosity, large surface area, and biocompatibility, zeolites are widely employed as drug delivery carriers since they have proven to be ideal hosts for organic molecule encapsulation, including photoactive species [[2], [3], [4], [5]]. The first step in the preparation of zeolite/organic molecule hybrid materials is the dehydration of the zeolite to facilitate the penetration of the desired molecules. Consequently, it is essential to thoroughly investigate how H_2O is released, at what temperature, and how this affects the zeolite framework.

Many studies and reviews report the thermally induced dehydration and consequent structural deformations of alumino-silicate hydrated phases, see e.g. Refs. [6,7]. In general, it is widely accepted that: a) thermal stability increases with Si/Al ratio as a consequence of the higher energy required to break the Si–O bond compared to the

Al–O bond; b) lower dehydration temperatures are observed in zeolites with higher Si/Al ratios since their surfaces become more hydrophobic. On the basis of the collapse temperature obtained by X-ray structural investigations, Cruciani [6] introduced the so-called "stability index" (SI) and demonstrated a clear correlation between SI and the Si/(Si + Al) ratio.

Several data sets are also available on the thermal behavior of pure and high silica phases [[8], [9], [10], [11], [12], [13], [14]]. Since most high silica zeolites are obtained by dealumination, their properties are affected by the presence of connection defects and their investigation assumes particular importance, especially if the SiOH connectivity can be defined. For most of these materials, the silicatic framework undergoes negative thermal expansion (NTE) of variable entity.

This work aims to define thermal stability, heat-induced structural deformations, and reversibility of these processes in a high silica mordenite. This phase has proven to be an ideal host for the encapsulation of several kinds of organic molecules (hydrocarbons, ethylene glycol, etc.), e.g. Refs. [[15], [16], [17]], and is a promising scaffold for several other applications in the drug delivery field. For the reasons set out above, understanding framework modifications of high silica mordenite under preloading treatment (i.e. high temperature) is of great importance.

2. Experimental methods

2.1. Material

High silica mordenite (HS-MOR) with an SiO_2/Al_2O_3 molar ratio of 220, was purchased (code HSZ-690HOA) in its protonated form from Tosoh Corporation (Japan). This material was previously characterized by our group by different techniques (SEM, surface area, porosimetric analysis, thermogravimetric analysis, and FTIR spectroscopy) [17] and was used in previous work on the adsorption of pollutants from waste water [15,16,[18], [19], [20], [21]]. FTIR spectroscopy revealed the presence of a large quantity of silanol defects produced by the dealumination process. The nominal particle size is 10 μm.

Mordenite (framework type MOR [22]) crystal structure exhibits a 1D channel system characterized by two parallel channels running along the c axis, comprising a large 12 MR channel and a strongly elliptical 8 MR channel. These channels are

interconnected along the [010] direction through side pockets delimited by double 8 MRs that, in turn, form a sinusoidal channel running parallel to the b axis [23].

2.2. Infrared spectroscopy in controlled atmosphere

The infrared measurements were carried out on a PerkinElmer 2000 spectrophotometer equipped with Globar source and MCT detector, operating at a resolution of 2 cm^{-1} and averaging 64 scans for each spectrum collected. The zeolite powder was compressed into a self-supporting pellet and enclosed in a gold-frame, then inserted into a traditional quartz-glass infrared cell where both the thermal treatment and infrared analysis were conducted. The cell was closed and connected to a vacuum line (residual pressure 5.0×10^{-4} mbar). The thermal treatment consisted of heating the material in dynamic vacuum from rT to 800 °C for 30 min. Isotopic exchange was achieved by exposing the outgassed material to D_2O vapor pressure for 5 cycles of 5 min.
The Fit Curve routine of Bruker's OPUS 5.0 software was used to fit the νOH experimental profile.

2.3. Thermogravimetric (TG) analysis

TG analysis of HS-MOR was made using a Seiko SSC/5200 thermal analyzer. About 10 mg of the sample was loaded into a Pt crucible and heated in air from room temperature to 1050 °C, at a heating rate of 10 °C/min, the same heating rate used for in-situ XRPD collections.

2.4. Synchrotron X-ray powder diffraction (XRPD) experiments

The temperature-resolved synchrotron XRPD patterns were collected at ID22 beamline at ESRF (Grenoble) at a fixed wavelength of 0.3544 Å. The wavelength was calibrated with Si NIST standard reference material. The powder sample was loaded and packed into a 0.5 μm quartz capillary. The capillary was mounted on a standard goniometric head and kept spinning during pattern collection. The sample was heated in situ using a hot-air blower from rT to 800 °C at a heating rate of 10 °C/min.

Temperature was calibrated against the thermal expansion of a standard Pt reference material. Diffraction patterns were recorded with a high-resolution multi-analyzer stage composed of nine analyzer crystals in the 2θ range 0–25°. Between 50 and 600 °C the patterns were collected every 50 °C, while above 600 °C every 100 °C. During temperature decrease, two data collections were performed at 150 °C and room temperature (labeled 150 °C$_{rev}$ and rT_{rev}, respectively).

2.5. Structure refinements

The GSAS package [24] with the EXPGUI interface [25] was used for Rietveld structure refinements. The starting coordinates adopted and site labels are from Ref. [17]. The refinements were tested in both *Cmcm* and *Cmc2$_1$* s g. The *Cmc2$_1$* s g. refinements were found to be more satisfactory and hence this space group was adopted for all the investigated temperatures (only *Cmc2$_1$* data are here reported). The Bragg-peak profiles were modeled by a pseudo-Voigt function [26] with a peak intensity cut-off set to 0.001 of the peak maximum. A 24-term Chebyshev polynomial was used to fit the background curve. The overall scale factor, the 2θ-zero shift, and the unit-cell parameters were refined for each histogram over the entire temperature range. Si^{4+} and O^{2-} scattering curves were used for the framework species, and the O^{2-} used again for H$_2$O molecules. Soft constraints were imposed on the tetrahedral bond lengths T-O (1.63 Å), with a tolerance value of 0.03 Å. Isotropic thermal displacement parameters were constrained to the same value for the same atomic species.

The refinement details at selected temperatures (rT, 300, 800 °C, and rT_{rev}) are summarized in Table 1. The final observed and calculated patterns for the selected refinements are shown in Fig. 2S a,b,c,d of the Supplementary Materials. Table 1, Table 2S respectively report the atomic coordinates and bond distances. Table 2 reports the unit-cell parameters refined for all the investigated temperatures.

Table 1. Unit-cell parameters and details of structural refinements at selected temperatures.

T (°C)	rT	300	800	rT_{rev}
Space group	*Cmc2$_1$*	*Cmc2$_1$*	*Cmc2$_1$*	*Cmc21*
a (Å)	18.0609(2)	18.0440(2)	17.9394(4)	17.9881(5)

T (°C)	rT	300	800	rT_{rev}
b (Å)	20.2095(2)	20.1824(2)	19.9711(4)	20.0432(5)
c (Å)	7.4546(1)	7.4470(1)	7.3943(2)	7.4111(2)
V (Å³)	2720.9(1)	2712.0(1)	2649.2(1)	2672.0(2)
R_p (%)	5.70	6.05	5.11	5.07
R_{wp} (%)	7.26	7.69	6.65	6.65
R F**2 (%)	7.59	7.21	8.01	6.62
No. of variables	114	91	91	91
No. of observations	11601	10933	7946	7946
No. of reflections	1411	1202	539	559

Table 2. Cell parameters of HS-MOR at all the investigated temperatures.

T (°C)	Space group	a (Å)	b (Å)	c (Å)	V (Å³)
RT	$Cmc2_1$	18.0609(2)	20.2095(2)	7.4546(1)	2720.9(1)
50	$Cmc2_1$	18.0598(2)	20.2058(2)	7.4542(1)	2720.1(1)
100	$Cmc2_1$	18.0658(2)	20.2115(2)	7.4539(1)	2721.7(1)
150	$Cmc2_1$	18.0609(2)	20.2095(2)	7.4532(1)	2720.4(1)
200	$Cmc2_1$	18.0553(2)	20.2015(2)	7.4518(1)	2718.0(1)
250	$Cmc2_1$	18.0500(2)	20.1919(2)	7.4499(1)	2715.2(1)
300	$Cmc2_1$	18.0440(2)	20.1824(2)	7.4470(1)	2712.0(1)
350	$Cmc2_1$	18.0379(3)	20.1728(2)	7.4438(1)	2708.6(1)
400	$Cmc2_1$	18.0309(2)	20.1612(2)	7.4403(1)	2704.7(1)
450	$Cmc2_1$	18.0227(2)	20.1474(2)	7.4361(1)	2700.1(1)
500	$Cmc2_1$	18.0142(2)	20.1330(2)	7.4319(1)	2695.4(1)
550	$Cmc2_1$	18.0040(3)	20.1138(2)	7.4269(1)	2689.5(1)
600	$Cmc2_1$	17.9924(3)	20.0899(3)	7.4212(1)	2682.5(1)
700	$Cmc2_1$	17.9631(3)	20.0280(3)	7.4071(1)	2664.8(1)
800	$Cmc2_1$	17.9394(4)	19.9711(4)	7.3943(2)	2649.2(1)
150 rev.	$Cmc2_1$	17.9814(5)	20.0333(5)	7.4095(2)	2669.1(2)
RT rev.	$Cmc2_1$	17.9881(5)	20.0432(5)	7.4111(2)	2672.0(2)

3. Results and discussion

3.1. Infrared spectroscopy in controlled atmosphere

shows the IR spectra of HS-MOR at increasing dehydration/dehydroxylation steps for the ranges in which signals were observed deriving from OH stretching (νOH) of silanols and H_2O molecules (section A), and overtone/combination bands of lattice modes and H_2O (δH_2O) molecule deformation band (section B).

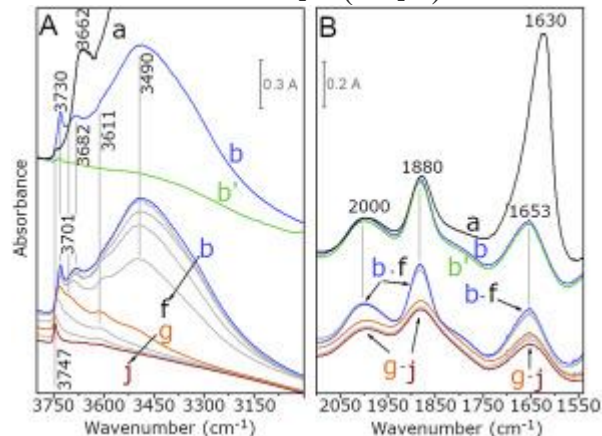
Fig. 1. Infrared spectra in the νOH (A) and overtone/combination lattice modes and δH_2O (B) regions of: HS-MOR in air (a) and outgassed from rT (b) up to 800 °C (j) in steps of 100 °C. Curve b': HS-MOR after H/D isotopic exchange by contact with D_2O at vapor pressure at rT and subsequent outgassing. The signal of the sample in air (a) is out of scale because of the large amount of H_2O molecules present in the system.
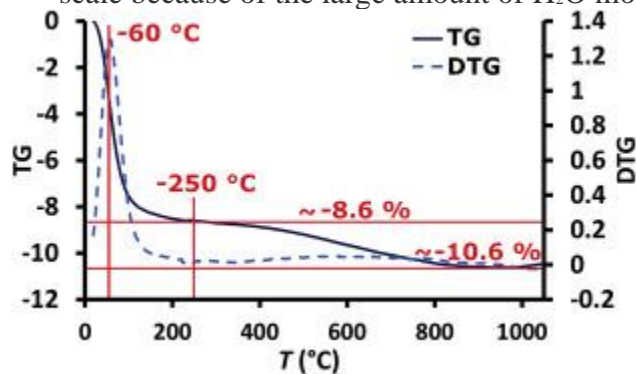

Fig. 2. TG and DTG curves of HS-MOR.

For the material in air (curve a), most of the νOH signal is out of scale (section A), because of the large number of H_2O molecules present in the system. The only observable features are at 3662 cm⁻¹, caused by the stretching of OH moieties without interaction with other H_2O molecules [27], along with a weak component at 3747 cm⁻¹, due to highly hydrophobic isolated silanols unable to adsorb H_2O molecules at the relative humidity of the ambient conditions during the measurement.

At lower frequency (section B), the spectrum of the material in air is dominated by a peak at 1630 cm⁻¹ due to the δH_2O of adsorbed molecules, accompanied by signals at

2000 and 1880 cm^{-1}, resulting from lattice mode combinations, while a partner signal resulting from an overtone of lattice modes expected at ca. 1650 cm^{-1} is obscured by the δH$_2$O mode [28]. The disappearance of the δH$_2$O band at 1630 cm^{-1} after outgassing under high vacuum at rT for 30 min (curve b), now revealing an overtone at 1653 cm^{-1}, testifies the removal of adsorbed H$_2$O molecules. The completeness of desorption is proven by the invariance of the spectral profile in the 1700-1600 cm^{-1} range of the sample after H/D isotopic exchange (curve b') by contact with D$_2$O at vapor pressure at rT, which should have depleted any δH$_2$O component (converted to a lower frequency δD$_2$O signal), if still present after outgassing. Regarding the νOH region (section A), the spectral profile remaining after water desorption (curve b) is due only to hydroxy groups, overwhelmingly silanols, ≡SiOH, because of the very high Si/Al ratio. Only traces of hydroxy group patterns are still present in the spectrum of the H/D exchanged sample (curve b') indicating that almost all of them are accessible to H$_2$O molecules (when dosed at water vapor pressure at rT). For the sample in air, all signals due to hydroxy groups were displaced towards lower frequencies by the interaction with H$_2$O (except for a small fraction due to highly hydrophobic isolated silanols), and then hidden by the νOH band of H$_2$O molecules.

In more detail, the outgassed sample pattern is dominated by a broad band with maximum at 3490 cm^{-1}, typical of H-bonded silanols like those in so-called "silanol nests" and expected in highly dealuminated zeolites [29]. An ill-resolved shoulder at 3611 cm^{-1} can be attributed to Brønsted acid ≡Si-(OH)-Al≡ sites [30], while components at 3682, 3701, and 3730 cm^{-1} are due to silanols involved in interactions becoming weaker as the νOH frequency rises [28]. Finally, the presence of isolated silanols, evidenced by the component at 3747 cm^{-1} in curve a, should contribute to the high frequency side of the 3730 cm^{-1} band.

The intensity of the overall νOH pattern decreases as the outgassing temperature is increased up to 800 °C (curve j), leaving a more intense component at 3747 cm^{-1}, indicating some increase in the quantity of isolated silanols (curves b-j). As a whole, this evolution indicates a progressive condensation of hydroxyl groups forming Si–O–Si linkages in the case of silanols.

It is noteworthy that two different regimes can be observed as a function of temperature. The components at 3490 cm^{-1} and 3682 cm^{-1} exhibit the largest decrease

in intensity when the outgassing temperature is increased from 400 to 500 °C (curves f, g), while most of the decline in other components occurs at higher temperatures (curves g-j). This behavior is consistent with the strength of the inter-silanol interactions, directly proportional to their distance. Indeed, the shorter the distance (i.e. silanols with νOH 3490 and 3682 cm^{-1}), the easier the condensation between silanols, which therefor occur at lower temperatures.

The thermogravimetric data presented below indicate that the hydroxyl groups might be ca. 6 p.u.c. in the pristine HS-MOR. To establish a relative quantification of the various types of hydroxy groups contributing to the νOH pattern, the experimental profile in the 3800–3000 cm^{-1} range was fitted. The integrated intensity of the resulting components were recalculated on the basis of the relationship between OH stretching frequency and the relative decadic absorption coefficient proposed by Carteret [31], making it possible to take into account the increase in this coefficient as the strength of the inter-silanols interaction increases [31]. The data analysis results are reported in Fig. 1S, indicating that the silanols responsible for the components at 3490 and 3682 cm^{-1} account for ca. 90% of hydroxy groups. Clearly, condensation of this number of silanols has an impact on the zeolite lattice, as evidenced by the changes in the combination and overtone modes responsible for the bands at 2000, 1880, and 1653 cm^{-1} when the outgassing temperature was increased from 400 to 500 °C (curves f, g in section B of Fig. 1).

3.2. Thermogravimetric analysis

Fig. 2 shows the thermogravimetric analysis results. As highlighted by the DTG curve, weight-loss starts at very low temperatures, with the main weight-loss at about 60 °C. At 250 °C the TG curve indicates a weight-loss of 8.6%. Above this temperature, a continuous slow weight loss leads to a total loss of 10.6%.

The initial weight loss, between rT and 250 °C, can be ascribed to the release of H_2O molecules from the zeolite porosity/surface, and corresponds to 15.1H_2O p.u.c. The main weight loss in this range is at low temperature and is due to weakly bonded H_2O present in the channels and/or on the zeolite surface, as evidenced by the infrared spectra of the outgassing process at rT. The remaining 1.72%, lost at higher

temperatures (400–900 °C), is consistent with IR results and corresponds to the H_2O release resulting from silanol condensation.

3.3. Structure refinements

3.3.1. Structure of HS-MOR at room conditions

The structure refinement of HS-MOR at room conditions indicates the presence of seven partially occupied H_2O sites, corresponding to $10.34H_2O$ molecules p.u.c. The difference between this value and that resulting from the TG analysis (15.1 molecules) can be ascribed to the presence of disordered and lowly occupied sites not identifiable in the refinement, and/or to the contribution of H_2O molecules physiosorbed on the surface. The structure derived from the refinement at rT is reported in Fig. 3 a, b, and in Table 1, Table 2S.
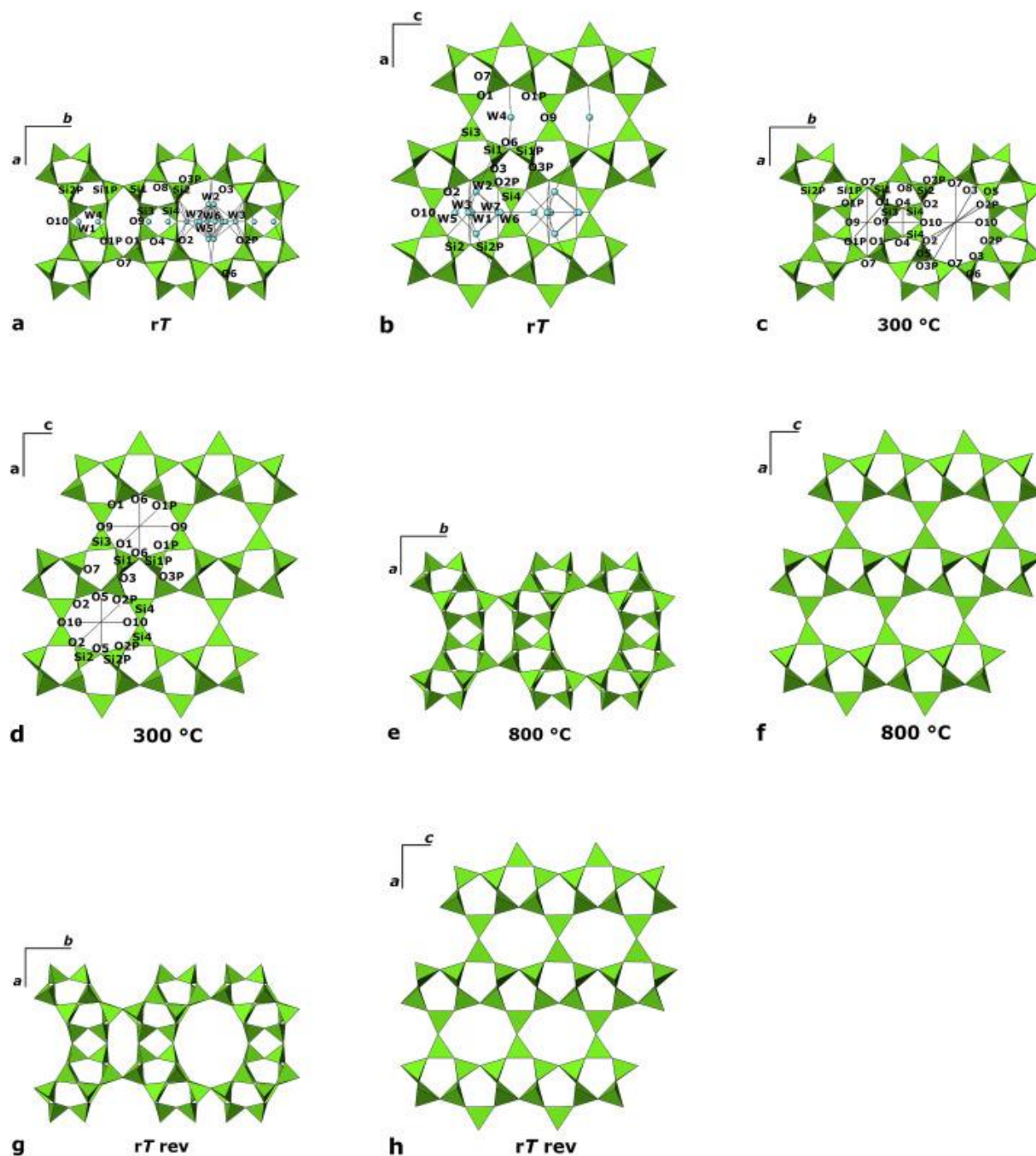
Fig. 3. Projection along [001] and [010] of HS-MOR structure at rT (a,b), 300 (c,d) 800 °C (e,f), and rT_{rev} (g,h).

The W2, W3, W5, W6, and W7 sites are mainly 12 MR channels parallel to [001], while W1 and W4 are in the side pocket. All H_2O molecules, with the exception of those in W2, are sited on the mirror plane perpendicular to the a axis (Table 1S and Fig. 3). W1 is near to site D' found in natural mordenite from Pashan $((Na_{3.51}K_{0.14}Ca_{1.89}Mg_{0.09}Sr_{0.01}) [Fe^{3+}_{0.03}Al_{7.40}Si_{40.53}O_{96}] \cdot 27.26H_2O)$ [32], W2 is near to site E,

W3 to D, W4 to B, and W6 to site F. Site G in the Pashan sample is close to the W5 and W7 sites of HS-MOR, which are almost equivalent in *Cmcm* s.g.

In general, the structure refinement at r*T* shows that H_2O molecules are weakly or not bonded to the framework oxygen atoms (distance ~3.25 Å), with the exception of W7, which is strongly bonded (2.61(8) Å) to O10 (Table 2S). This H_2O molecule's distribution is consistent with the TG analysis, justifying the large weight loss observed at low temperature, and with IR data under degassing.

3.3.2. Cell parameter behavior

The structural refinements of HS-MOR in the *Cmc2₁* s g. were successful at all the investigated temperatures. Details of the Rietveld refinement parameters at r*T*, 300, 800 °C, and r*T*$_{rev}$ are reported in Table 1. No phase transitions or symmetry changes were observed with increasing temperature and the zeolite was stable up to 800 °C. Some diffraction peaks were broadened at the tails, and this led to a misfit in intensities between observed and calculated patterns after Rietveld refinement. This effect was particularly marked for peak (111), which could be due to framework defectiveness, probably induced by the dealumination procedure. Similarly, Simoncic and Armbruster [33] reported the presence of diffuse scattering in both natural and synthetic mordenite due to disorder in the MOR framework.

Fig. 4 reports the evolution of the HS-MOR lattice parameters with *T*. The unit cell parameters show very slow and almost isotropic changes upon heating.

The *c* parameter decreases right across the studied *T* range, while *a* and *b* undergo a very small decrease below 50 °C, followed by an increase to values slightly higher than those observed at r*T*. Above 100 °C, and up to 800 °C, all parameters shrink. Above 550 °C an increase in slope is observed for all parameters. This corresponds to marked silanol condensation and resulting framework modification, also highlighted by changes in the combination and overtone modes of the infrared bands. The overall lattice contractions are 0.67%, 1.18%, and 0.81% for *a*, *b*, *c*, respectively, and 2.64% for cell volume.
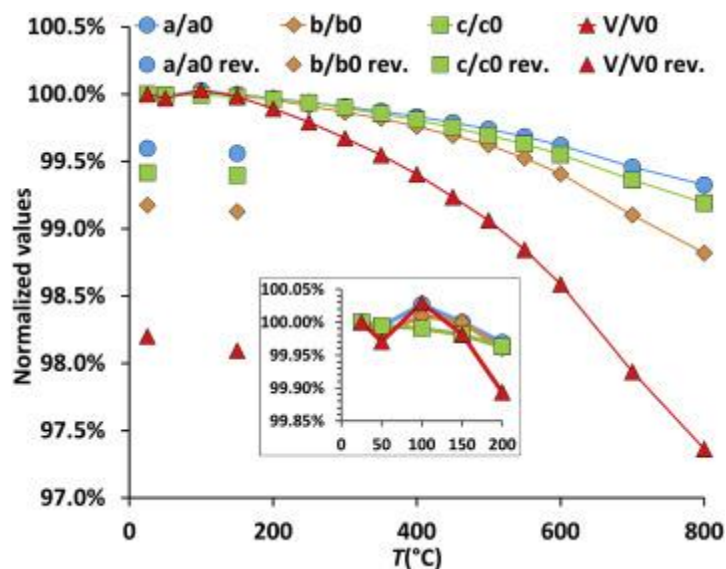
Fig. 4. Normalized unit-cell parameters of HS-MOR *vs.* temperature.

The odd trend in HS-MOR parameters between r*T* and 100 °C corresponds to the main dehydration step observed in the TG curve (Fig. 2). The expansion of *a* and *b* between 50 and 100 °C can thus be explained as a response of the framework to the H_2O flow through the 12 MR and 8 MR channels. A comparable "breathing" effect was found in analcime [34], where the six-member ring apertures of the channels parallel to (111) are opened as widely as possible during dehydration. During HS-MOR cooling, the unit cell does not recover its original dimensions, but maintains - at both 150 °C$_{rev}$ and r*T*$_{rev}$ - values close to those found at 700 °C. Comparing the variation of the unit cell parameters of HS-MOR with those of Pashan mordenite [32], it is possible to identify some differences in thermal behavior. The cell volume contraction of the natural sample (~1.9% mainly due to *b* parameter decrease) is lower than that observed for HS-MOR. This is clearly due to the presence of extraframework cations, which sustain the framework during dehydration. In general, the high stability and low deformability of the MOR structure under heating is confirmed even in the high-silica sample.

3.3.3. H_2O release induced by heating

Fig. 5 reports the variation in the number of H_2O molecules at the different W sites. The sample weight loss in the range r*T*-300 °C is also shown for comparison. A decrease in occupancy factors for almost all the H_2O sites is observed during the initial heating stage, thus confirming the TG data that indicate dehydration already

starts between rT and 50 °C. Only the W3 and W7 sites show a slightly higher occupancy at 50 °C with respect to rT, favored by the better coordination of these sites with the framework oxygens. At 100 °C the H_2O molecules at W2, W5, and W7 hosted in the 12 MR channel are completely lost. Subsequently, in the range 100–150 °C, the molecules at W1 and W6, respectively located near the middle of the side pocket and of the 12 MR channel, are removed, while the W3 and W4 molecules remain in the center of the 8 MR windows of the side pocket, coordinated to framework oxygen atoms. At 200 °C even W4 is completely lost and only 0.6H_2O molecules persist at the W3 site. Dehydration is complete at 300 °C.
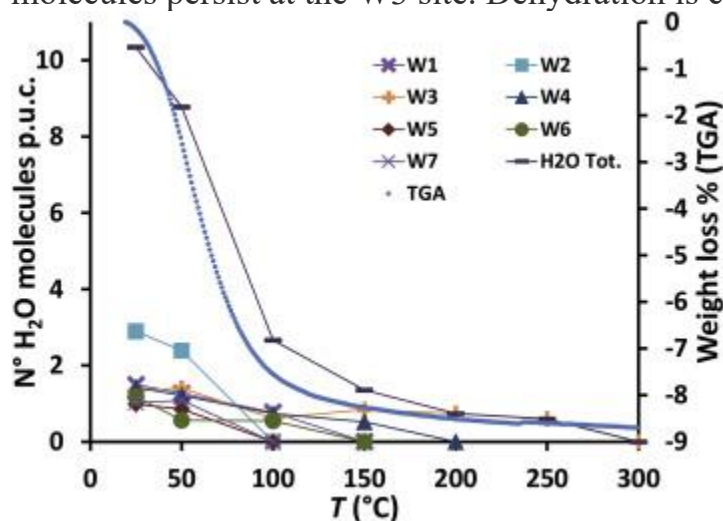

Fig. 5. Total H_2O content per unit cell and for each extraframework site *vs*. temperature compared with the TG curve.

Infrared characterization revealed that the desorption of adsorbed H_2O molecules by degassing is already complete at rT. It is worth noting that the evolution of the H_2O and hydroxy group content revealed with infrared spectra was obtained by outgassing HS-MOR at various temperatures in a dynamic vacuum regime, while the XRPD experiments were carried out under static pressure conditions that discourage H_2O diffusion.

3.3.4. Framework structural distortions induced by heating

Fig. 3 shows the refined structure of HS-MOR at rT, 300 °C, 800 °C, and rT_{rev}, viewed along [001] (a, c, e, g) and [010] (b, d, f, h).

The small unit cell volume contraction observed in the investigated T range is mainly due to a decrease in the b parameter, which starts above 150 °C (Fig. 4) and is

enhanced at about 550 °C. The shrinking of b is related to the deformation of the 8 MR channel aperture. Fig. 3 c and e show the decrease in the O9–O1–O7 angle, which induces a strong deformation of the 8 MR. Summarizing, HS-MOR undergoes very moderate T induced deformations, which indicates a very rigid and stable framework.

3.3.5. Thermal expansion

The thermal behavior of HS-MOR can be described using thermal expansion coefficients:

i)

Between rT and 300 °C (temperature at which all the H_2O molecules are released), the values are -2.19×10^{-6} K^{-1}, -3.17×10^{-6} K^{-1}, -2.29×10^{-6} K^{-1}, -7.62×10^{-6} K^{-1}, for a, b, c, and V, respectively;

ii)

Between 300 and 800 °C the values are -11.59×10^{-6} K^{-1}, -20.94×10^{-6} K^{-1}, -14.15×10^{-6} K^{-1}, -46.31×10^{-6} K^{-1} for a, b, c, V, respectively.

These results appear to indicate that HS-MOR undergoes a negative thermal expansion (NTE) above 300 °C. However, this interpretation is not strictly rigorous, since the sample's weight loss, associated to the release of hydroxyls, continues up to the highest investigated temperature (Fig. 2). It is likely that the condensation of silanols, with the formation of siloxane bridges between silica tetrahedra, contributes to the shrinkage of cell parameters.

Negative thermal expansion (NTE) is defined as a reversible contraction of the material unit cell upon heating, and it was originally determined in structures with M-O-M linkages like metal oxides [[35], [36], [37]]. Recently, NTE was observed in the dehydrated forms of many microporous materials with Si–O–Si linkages [6,11,38]. Most of the high silica synthetic zeolites, with 2D or 3D channel system, exhibit this thermal behavior. In open frameworks like zeolites, the main mechanism was explained by Sleight [35] as the presence of transverse thermal vibrations of the oxygen atoms in Si–O–Si linkages. These motions may occur cooperatively and large void volumes are required to accommodate the cooperative rotations of tetrahedra. Since the thermal expansion of the tetrahedra is negligible, they are free to rotate as

rigid units with little or no internal distortions. This mechanism has been justified on the basis of the so-called rigid unit mode (RUM) model [39]. The increase in vibrational amplitude of RUMs as a function of temperature is thus the underlying mechanism of NTE in framework structures ([40] and references therein). Based on lattice dynamics calculations for 18 siliceous and non-siliceous zeolites, Tschaufeser and Parker [41] suggested that NTE is more the norm rather than the exception for these materials.

It is clear that the condensation of silanols induces the rotation of the corresponding tetrahedra to establish new Si–O–Si bonds. This phenomenon explains both the shrinkage of the cell lattice (the "apparent" NTE), and the failed recovery of original cell values by HS-MOR during cooling (150 °C$_{rev}$ and rT_{rev}). The HT induced condensation of silanols does not allow their complete rehydration, thus hindering complete recovery of the initial cell volume.

4. Concluding remarks

Strictly following Baur's classification [42], HS-MOR can be defined as flexible and collapsible, similarly to natural mordenite.

This phase is a very thermally stable zeolite, since up to at least 800 °C it does not undergo phase transition or amorphization, and overall unit cell contraction is less than 3%. The Stability Index (SI) - as defined by Cruciani [6] is 5, corresponding to the temperature of structural breakdown > 800 °C. This result was reasonably predictable, due to: i) the high Si/Al ratio (~110); ii) the high energy required to break the Si–O bond; iii) the presence of columns of five and four-membered rings that stiffen the framework [43,44].

The thermal expansion coefficients seem to indicate that HS-MOR undergoes a negative thermal expansion (NTE) above 300 °C. However, this interpretation is not strictly rigorous, since the sample's weight loss, associated with the release of H_2O molecules due to the condensation of silanols (widely present in this dealuminated sample) continues up to the highest investigated temperature.

Overall, all the data indicated a weak interaction of the H_2O molecules with the high silica mordenite framework, and provided evidence for the presence of different types of hydroxy groups with their different responses to thermal condensation. Infrared

characterization showed that the desorption of adsorbed H_2O molecules by degassing is already complete at rT.

This interpretation of all the observed data might provide some insight into the thermal behaviour of other dealuminated zeolitic materials.

Declaration of competing interest

The authors declare that they have no known competing financial interests or personal relationships that could have appeared to influence the work reported in this paper.

Acknowledgements

References

[1]

S.M. Csicsery

Zeolites, 4 (1984), pp. 202-213

[2]
L. Gigli, R. Arletti, J.G. Vitillo, G. Alberto, G. Martra, A. Devaux, G. Vezzalini

J. Phys. Chem. C, 119 (2015), pp. 16156-16165

[3]
G. Calzaferri, D. Bruhwiler, S. Megelski, M. Pfenniger, M. Pauchard, B. Hennessy, H. Maas, A. Devaux, U. Graf

Solid State Sci., 2 (2000), pp. 421-447

[4]
M. Polisi, R. Arletti, S. Morandi, M. Fabbiani, G. Martra, S. Quartieri, L. Pastero, G. Vezzalini

Microporous Mesoporous Mater., 268 (2018), pp. 25-30

[5]

H. Lulf, A.e. Devaux, E.A. Prasetyanto, L. De Cola**Porous nanomaterials for biomedical applications**
T. Torres, G. Bottari (Eds.), Organic Nanomaterials, Wiley, New York (2013), pp. 487-507

[6]

G. Cruciani

J. Phys. Chem. Solids, 67 (2006), pp. 1973-1994

[7]

D.L. Bish, J.W. Carey

Natural Zeolites: Occurrence Prop. Appl., 45 (2001), pp. 403-452

[8]

P. Lightfoot, D.A. Woodcock, M.J. Maple, L.A. Villaescusa, P.A. Wright

JMCh, 11 (2001), pp. 212-216

[9]

M.M. Martinez-Inesta, R.F. Lobo

J. Phys. Chem. B, 109 (2005), pp. 9389-9396

[10]

T. Carey, A. Corma, F. Rey, C.C. Tang, J.A. Hriljac, P.A. Anderson

Chem. Commun., 48 (2012), pp. 5829-5831

[11]

L. Leardini, S. Quartieri, G. Vezzalini, R. Arletti

Microporous Mesoporous Mater., 202 (2015), pp. 226-233

[12]

S.H. Park, R.W.G. Kunstleve, H. Graetsch, H. Gies, H. Chon, S.K. Ihm, Y.S. Uh

Prog. Zeolite Microporous Mater. Pts a-C, 105 (1997), pp. 1989-1994

[13]

D.S. Bhange, V. Ramaswamy

Microporous Mesoporous Mater., 103 (2007), pp. 235-242

[14]

D.S. Bhange, V. Ramaswamy

Microporous Mesoporous Mater., 130 (2010), pp. 322-326

[
1
5
]

A. Martucci, L. Pasti, M. Nassi, A. Alberti, R. Arletti, R. Bagatin, R. Vignola, R. Sticca

Microporous Mesoporous Mater., 151 (2012), pp. 358-367

R. Arletti, A. Martucci, A. Alberti, L. Pasti, M. Nassi, R. Bagatin

J. Solid State Chem., 194 (2012), pp. 135-142

R. Arletti, L. Leardini, G. Vezzalini, S. Quartieri, L. Gigli, M. Santoro, J. Haines, J. Rouquette, L. Konczewicz

Phys. Chem. Chem. Phys., 17 (2015), pp. 24262-24274

[18]

A. Martucci, L. Pasti, N. Marchetti, A. Cavazzini, F. Dondi, A. Alberti

Microporous Mesoporous Mater., 148 (2012), pp. 174-183

A. Martucci, M.A. Cremonini, S. Blasioli, L. Gigli, G. Gatti, L. Marchese, I. Braschi

Microporous Mesoporous Mater., 170 (2013), pp. 274-286

V. Sacchetto, G. Gatti, G. Paul, I. Braschi, G. Berlier, M. Coss, L. Marchese, R. Bagatin, C. Bisio

Phys. Chem. Chem. Phys., 15 (2013), pp. 13275-13287

S. Blasioli, A. Martucci, G. Paul, L. Gigli, M. Cossi, C.T. Johnston, L. Marchese, I. Braschi

J. Colloid Interface Sci., 419 (2014), pp. 148-159

C.M. Baerlocher, B. Lynne, D.H. Olson**Atlas of Zeolite Framework Types**
(sixth ed.), Elsevier, Amsterdam, The Netherlands (2007)

W.M. Meier

Z. für Kristallogr. - Cryst. Mater., 115 (1961), pp. 439-450

A.C. Larson, R.B. Von Dreele

Los Alamos National Laboratory Report LAUR, vols. 86–748 (2000)

B.H. Toby

J. Appl. Crystallogr., 34 (2001), pp. 210-213

P. Thompson, D.E. Cox, J.B. Hastings

J. Appl. Crystallogr., 20 (1987), pp. 79-83

M. Takeuchi, L. Bertinetti, G. Martra, S. Coluccia, M. Anpo

Appl. Catal. Gen., 307 (2006), pp. 13-20

A. Burneau, J.P. Gallas**Vibrational spectroscopies**
A.P. Legrand (Ed.), The Surface Properties of Silicas, Wiley & Sons, Chichester (1998), p. 181

T. Kawai, K. Tsutsumi

J. Colloid Interface Sci., 212 (1999), pp. 310-316

C. Bisio, G. Martra, S. Coluccia, P. Massiani

J. Phys. Chem. C, 112 (2008), pp. 10520-10530

C. Carteret

J. Phys. Chem. C, 113 (2009), pp. 13300-13308

A. Martucci, M. Sacerdoti, G. Cruciani, C. Dalconi

Eur. J. Mineral., 15 (2003), pp. 485-493

P. Simoncic, T. Armbruster

Am. Mineral., 89 (2004), pp. 421-431

G. Cruciani, A. Gualtieri

Am. Mineral., 84 (1999), pp. 112-119

A.W. Sleight

Curr. Opin. Solid State Mater. Sci., 3 (1998), pp. 128-131

J.S.O. Evans

J. Chem. Soc. Dalton Trans. (1999), pp. 3317-3326

G.D. Barrera, J.A.O. Bruno, T.H.K. Barron, N.L. Allan

J. Phys-Condens. Mat., 17 (2005), pp. R217-R252

W. Miller, C.W. Smith, D.S. Mackenzie, K.E. Evans

J. Mater. Sci., 44 (2009), pp. 5441-5451

K.D. Hammonds, A. Bosenick, M.T. Dove, V. Heine

Am. Mineral., 83 (1998), pp. 476-479

V. Heine, P.R.L. Welche, M.T. Dove

J. Am. Ceram. Soc., 82 (1999), pp. 1793-1802

P. Tschaufeser, S.C. Parker

J. Phys. Chem., 99 (1995), pp. 10609-10615

W.H. Baur

J. Solid State Chem., 97 (1992), pp. 243-247

D.W. Breck**Zeolite Molecular Sieves, New York**
(1974)

J.V. Smith**Origin and structure of zeolites**
J.A. Rabo (Ed.), Zeolite Chemistry and Catalysis (1976), pp. 1-79